11th International Symposium on Turbulence and Shear Flow Phenomena (TSFP11)
Southampton, UK, July 30 to August 2, 2019

STRUCTURAL AND SPECTRAL ANALYSIS OF VARYING-PHASE OPPOSITION CONTROL IN TURBULENT CHANNEL FLOW

Simon S Toedtli
Graduate Aerospace Laboratories
California Institute of Technology
Pasadena, CA 91125, USA
stoedtli@caltech.edu

Christine H Yu
California Institute of Technology
Pasadena, CA 91125, USA
chyu@caltech.edu

Beverley J McKeon
Graduate Aerospace Laboratories
California Institute of Technology
Pasadena, CA 91125, USA
mckeon@caltech.edu

ABSTRACT

This study investigates the structural and spectral changes of a low Reynolds number turbulent channel flow due to varying-phase opposition control by means of direct numerical simulation. The focus is on three example controllers, each with a different phase shift in Fourier domain between sensor measurement and actuator response. Two of these controllers lead to drag reduction, while the third increases drag substantially. Based on snapshots of the flow structure and actuator response, as well as spatial spectra at various wall-normal planes, we show that drag reduced flows exhibit a strong imprint of the near-wall cycle in the control signal and that near-wall vortices are attenuated under these control schemes. In case of a drag increase, the control signal is much more multiscale and the most energetic scales are spanwise constant structures. In accordance with an increase in drag, these flows also show substantially more vortical activity, even far away from the wall. The present results suggest a range of spatial scales which may be used in the future to better understand the role of the phase and devise novel controllers with relaxed spatial resolution requirements.

INTRODUCTION

The potential benefits associated with targeted manipulations of turbulent flows have spurred vast research interest in the field of turbulent flow control over the past decades and brought forth numerous approaches for various control objectives and flow geometries (see for example Gad-el-Hak (2000) for an overview). Here, we concentrate on turbulent drag reduction in incompressible wall-bounded flows by means of active flow control and consider a variant of the well-known opposition control scheme (Choi *et al.* (1994)).

The opposition control scheme uses the wall-normal velocity (v) at a detection plane located at a distance y_d above the wall (denoted by y_w) as measurement input and generates blowing and suction with equal amplitude but opposite sign as actuator response at the wall, $v(y_w) = -v(y_d)$. Previous direct numerical simulation (DNS) studies of turbulent channel flow at $\mathrm{Re}_\tau = u_\tau h/\nu = 180$ (where u_τ is the friction velocity, h denotes the channel half-height and ν is the kinematic viscosity of the fluid) show that the attainable drag reduction (DR) strongly depends on the sensor location, with a maximum DR of approximately 25% (Choi *et al.* (1994)). Subsequent studies show that maximum drag reduction can be increased by using upstream sensor information (Lee (2015)) or adding an integral term to the control law (Kim & Choi (2017)) and that the effectiveness of control decreases with increasing Reynolds number (Deng *et al.* (2016)).

In this study, we consider opposition control from a Fourier domain rather than a physical domain perspective and we allow the controller gain, i.e. the proportionality constant between sensor measurement and actuator response (which was equal to -1 above), to be complex. We will refer to this control scheme as varying-phase opposition control hereafter and we will give a formal definition of the control law in the following section. Recent DNS results show that the DR attainable under varying-phase opposition control strongly depends on the phase of the complex controller gain and ranges from maximum DR for a slightly negative phase to substantial drag increase for positive phases (Toedtli *et al.* (2019)). However, it is yet to be understood how the structure of the flow changes with phase to bring about the observed variation in DR. The goal of the present study is therefore to shed light on the structural and spectral properties of controlled flows for various phases of the controller gain. We note that other questions about varying-phase opposition control, such as Reynolds number effects or net energy savings, also remain to be clarified, but such aspects are beyond the scope of this investigation.

APPROACH

In this study we investigate varying-phase opposition control in a low Reynolds number ($\mathrm{Re}_\tau \approx 180$) turbulent channel flow by means of DNS. The streamwise, wall-

normal and spanwise coordinate are denoted by x, y and z, respectively, with corresponding velocity components u, v and w. We will switch back and forth between a Fourier and physical domain representation of the streamwise and spanwise coordinate and in order to differentiate Fourier coefficients from physical domain quantities, we label the former with a superscript hat. The streamwise and spanwise wavenumbers are denoted by k_x and k_z, respectively, with corresponding wavelengths λ_x and λ_z.

The remainder of this section reviews the varying-phase opposition control law and summarizes the numerical framework used in this study. In the interest of brevity we only give an account of the most important aspects and interested readers may refer to Toedtli *et al.* (2019) for further details about the control scheme and the DNS.

Control Law

After a Fourier transform in the streamwise and spanwise direction, the varying-phase opposition control law can be written as

$$\hat{v}(k_x,k_z,y_w,t) = -\hat{A}_d\,\hat{v}(k_x,k_z,y_d,t-\Delta t) \tag{1}$$

where $\hat{A}_d \in \mathbb{C}$ is the complex controller gain and $\Delta t \in \mathbb{R}$ is a potential time delay between sensor measurement and actuator response. Note that the original opposition control scheme is recovered for $\hat{A}_d = 1$ and $\Delta t = 0$. The controller gain can be an arbitrary function of k_x and k_z, but in the absence of any structured dependence on k_x and k_z it is difficult to interpret its phase $\angle\hat{A}_d$ physically. In this study we wish to interpret the phase as a streamwise shift of the physical structure associated with a particular Fourier mode, which necessitates defining the controller gain as follows

$$\hat{A}_d = \begin{cases} 0, & \text{if } k_x = k_z = 0 \\ 1, & \text{if } k_x = 0, k_z \neq 0 \\ e^{i\phi}, & \text{if } k_x \neq 0, k_z = 0 \\ \frac{\min(|\hat{v}(k_x,k_z,t-\Delta t,y_d)|,|\hat{v}(k_x,-k_z,t-\Delta t,y_d)|)}{|\hat{v}(k_x,k_z,t-\Delta t,y_d)|}e^{i\phi}, & \text{otherwise} \end{cases} \tag{2}$$

where $\phi \in \mathbb{R}$. As explained in Toedtli *et al.* (2019), the above controller sets $\angle\hat{A}_d = 0$ if $k_x = 0$ (streamwise constant modes) and $|\hat{v}(k_x,k_z,y_w,t)| = |\hat{v}(k_x,-k_z,y_w,t)|$ if $k_x \neq 0$ in order to enable a clean interpretation of the phase as a streamwise shift $\Delta x = \phi/k_x$. A negative phase can be thought of as streamwise lead of the actuation, while a positive phase corresponds to a streamwise lag of the actuation relative to the sensor measurement. From here on, the term 'varying-phase opposition control' will be used to denote control law (1) with $\hat{A}_d$ according to Eq. (2). We would like to point out that this controller is related to the work of Lee (2015), but we apply a constant shift in Fourier domain rather than in physical domain.

The assumption of constant $\angle\hat{A}_d = \phi$ (for $k_x \neq 0$) across wavenumber space is made for simplicity. Note that the physical interpretation of the phase is also preserved if Eq. (2) is multiplied by a wavenumber-dependent factor $B(k_x,\pm k_z)e^{i\psi(k_x,\pm k_z)}$ with $\{B,\psi\} \in \mathbb{R}$, but controllers with such generalized gains are beyond the scope of this study. Further note that Eq. (2) selects the smaller of $|\hat{v}(k_x,k_z,y_d,t-\Delta t)|$ and $|\hat{v}(k_x,-k_z,y_d,t-\Delta t)|$ to generate the actuator response at $\hat{v}(k_x,\pm k_z,y_w,t)$, so that the control signal is always less energetic than the sensor measurement.

Direct Numerical Simulation

The varying-phase opposition control scheme introduced in the previous section is studied by means of DNS. The direct numerical simulations are performed with a code framework developed by Flores & Jiménez (2006) and the reader may refer to their manuscript for further details about the numerical method. The parameters of the DNS are chosen to match typical literature values: the size of the computational domain in the streamwise and spanwise direction is $L_x = 4\pi h$ and $L_z = 2\pi h$, respectively, and the resolution in these directions is $\Delta x^+ \approx 8.8$ and $\Delta z^+ \approx 4.4$, where the superscript $+$ denotes normalization with respect to viscous units of the uncontrolled flow, e.g. $\Delta x^+ = \Delta x(u_\tau)_0/\nu$. A sinusoidal grid is used in the wall-normal direction, with a resolution of $\Delta y^+_{\text{min}} \approx 0.37$ at the wall and $\Delta y^+_{\text{max}} \approx 3.09$ at the channel center. All control experiments are started from the same initial condition and statistics are collected over at least 10 eddy turnover times (h/u_τ) once a statistically steady state is reached. The adequacy of the DNS settings was confirmed by comparing results from the present DNS to literature data, see Toedtli *et al.* (2019) for more details.

The flow is driven by a constant mass flux, so that Re_τ, and therefore also the resolution in inner units, change when control is applied. The resolution increases if the drag is decreased and vice-versa and runs with $\text{Re}_\tau > 245$ may be considered slightly underresolved. Two runs with higher resolution were performed to rule out the possibility of grid effects in the results and it was indeed confirmed that the results were almost identical. It should also be noted that the varying-phase opposition control scheme is implemented as Dirichlet boundary condition. The sensor measurement from the previous timestep is used to generate the actuator response at the immediately following timestep, so that a delay of Δt is introduced in Eq. (1). Simulations with smaller Δt and therefore smaller delays were performed to rule out any effect of the delay and it was confirmed that the DR obtained for smaller Δt was essentially the same.

Since the mass flux is held constant, the change in drag due to control can be quantified in terms of relative change in mean wall shear stress τ_w

$$\text{DR} = 1 - \frac{(\tau_w)_c}{(\tau_w)_0} = 1 - \frac{(\text{Re}_\tau^2)_c}{(\text{Re}_\tau^2)_0} \tag{3}$$

where the subscript 0 and c label quantities of the uncontrolled and controlled flow, respectively. From here on, the term 'drag reduction' will be used to denote expression (3). Note that positive values indicate drag reduction, while negative values represent drag increase.

RESULTS

A total of 50 DNS runs covering a parameter range of five sensor locations, $y_d^+ = [5,10,15,20,25]$, and ten phase shifts, $\angle\hat{A}_d = [-3\pi/4, -\pi/2, -3\pi/8, -\pi/4, -\pi/8, 0, \pi/8, \pi/4, \pi/2, 3\pi/4]$ were performed to investigate the role $\angle\hat{A}_d$ in varying-phase opposition control. We first give a brief recap of how DR depends on the phase and readers may refer to Toedtli *et al.* (2019) for a more detailed discussion of this topic. We then focus on three example controllers and analyze the structural and spectral features of these controlled flows.

Recap of Drag Reduction Behavior

The dependence of the DR on the sensor location y_d and the phase between sensor and actuator $\angle\hat{A}_d$ is shown in Fig 1, which was obtained by interpolating the raw DR data from the 50 DNS runs using bilinear splines. Bright shading (positive numbers) represent drag reduction, while dark colors (negative numbers) indicate drag increase and the solid black lines outline a few selected contour levels. The dashed vertical line denotes varying-phase opposition control with $\angle\hat{A}_d = 0$, which up to the magnitude of the control input is equivalent to the original opposition control scheme (recall that $\hat{A}_d$ selects the smaller of $\hat{v}(k_x, \pm k_z, y_d, t-\Delta t)$ to set $|\hat{v}(k_x,k_z,y_w,t)| = |\hat{v}(k_x,-k_z,y_w,t)|$).

It is apparent that the effect of the controller strongly depends on the phase shift $\angle\hat{A}_d$ and generally speaking a small negative shift (e.g. $\angle\hat{A}_d = -\pi/4$) leads to improved drag reduction, while a positive phase shift deteriorates the control performance and eventually leads to drag increase. Furthermore, the map shows that for a fixed positive phase shift $0 < \angle\hat{A}_d$ the control performance decreases as y_d increases, while for a fixed negative phase shift $-\pi/2 \leq \angle\hat{A}_d < 0$ the control performance increases until it reaches a maximum and then decreases as the sensor moves away from the wall. Maximum DR of 21% is achieved for sensors located at $y_d^+ \approx 15$ and a phase shift $\angle\hat{A}_d = -\pi/4$. For reference, the controller with $\angle\hat{A}_d = 0$ and sensors located at the same $y_d^+ \approx 15$ achieves about 17% drag reduction, which shows that the introduction of a negative phase can improve the controller performance. Maximum drag increase occurs for large positive phase shifts and sensors located far away from the wall. In some of these cases drag increases by more than 400% or, equivalently, Re_τ increases by more than a factor of 2. It is also interesting to note that for a fixed sensor location, the phase can completely change the attainable DR: for example, a controller with sensors located at $y_d^+ \approx 15$ can achieve a 21% drag reduction if $\angle\hat{A}_d = -\pi/4$, while a controller with the same sensor location but a phase shift of $\angle\hat{A}_d = +\pi/2$ leads to a 180% drag increase.

We would also like to highlight some interesting connections to results in the literature: the DR behavior of the controller with zero phase shift ($\angle\hat{A}_d = 0$) as a function of y_d (dashed vertical line) agrees well with the results reported by Choi *et al.* (1994). It should be noted, however, that the maximum DR at $y_d^+ \approx 15$ of the present controller (approx. 17%) is lower than the 25% DR for classical opposition control reported in the literature. This difference is due to the smaller magnitude of the control input, as discussed previously. The conclusions drawn from Fig. 1 also agree well with the results of Lee (2015), who reports that the maximum DR can be increased by using upstream sensor information (negative phase), while DR decreases when the sensors are placed downstream (positive phase).

For the following structural and spectral analysis, we select three example controllers for further consideration. The example controllers are marked with a colored $\times$ in Fig. 1 and correspond to: $\angle\hat{A}_d = -\pi/4$ (controller leading to maximum DR), $\angle\hat{A}_d = 0$ (controller closely related to the original opposition control law) and $\angle\hat{A}_d = +\pi/2$ (example controller leading to substantial drag increase). In all three cases the sensors are located at $y_d^+ \approx 15$.

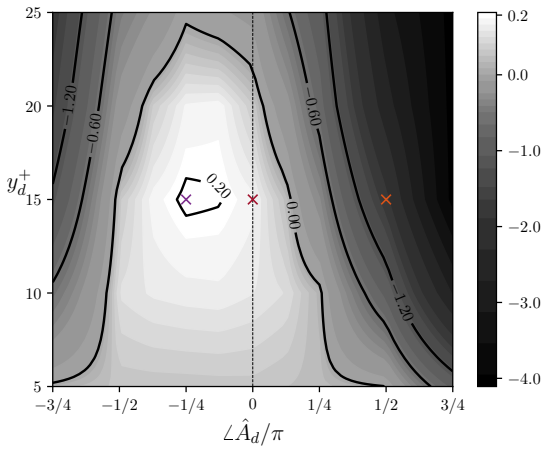

Figure 1: Contour map showing the drag reduction of varying-phase opposition control as a function of the sensor location y_d^+ and phase shift $\angle\hat{A}_d$. Positive numbers (light colors) indicate drag reduction, while negative numbers (dark colors) represent drag increase. The dashed vertical line denotes $\angle\hat{A}_d = 0$, which is closely related to the original opposition control scheme, and the markers ($\times$) indicate the example controllers considered subsequently. Note that the colorscale is nonlinear to highlight the region of drag reduction. Figure adapted from Toedtli *et al.* (2019).

Structural Analysis

Representative structural features of the three controlled flows are shown in Fig. 2. The left column displays streamwise wall-normal cross sections of vortical flow structures, which are identified by means of the λ_2-criterion (Jeong & Hussain (1995)). The threshold in all figures is $\lambda_2 = 0.05\,\lambda_u$, where $\lambda_u = -\max(|\lambda_2|_0)$ is the negative of the maximum absolute value of λ_2 of an uncontrolled flow at around the same instant in time. Figs. (2a) and (2c) look remarkably similar: the strongest vortical activity is found close to the wall and has a similar intensity in both figures. This suggests that the flow structure at maximum DR is not significantly different from classical opposition control. The controller with positive phase shift on the other hand draws a different picture: the vortical activity in Fig. (2e) is strongly enhanced and vortices are not only found in proximity of the wall, but throughout the channel. These observations confirm the intuition that vortices are less numerous in drag reduced flows and more abundant in drag enhanced configurations. It is interesting, however, to observe that the wall-based actuation does not only change the structure of the flow in proximity of the wall, but throughout (at least for $\angle\hat{A}_d = +\pi/2$.)

The right column of Fig. 2 shows instantaneous snapshots of the actuation at the wall. The velocities are made dimensionless with the centerline velocity of the uncontrolled flow at $\mathrm{Re}_\tau = 180$ and red indicates a positive v (blowing), while blue represents negative v (suction). Again we observe a close resemblance between the control input of $\angle\hat{A}_d = -\pi/4$ and $\angle\hat{A}_d = 0$: the wall actuation is dominated by a few spatial scales, which give rise to streamwise elongated streaky regions of positive and negative v. Typically, a region of positive v is surrounded on both sides (in the spanwise direction) by regions of negative v and vice-versa. One may speculate that the structure in the control signal is the imprint of the streamwise vortices detected at the sensor location and the spectral analysis in the follow-

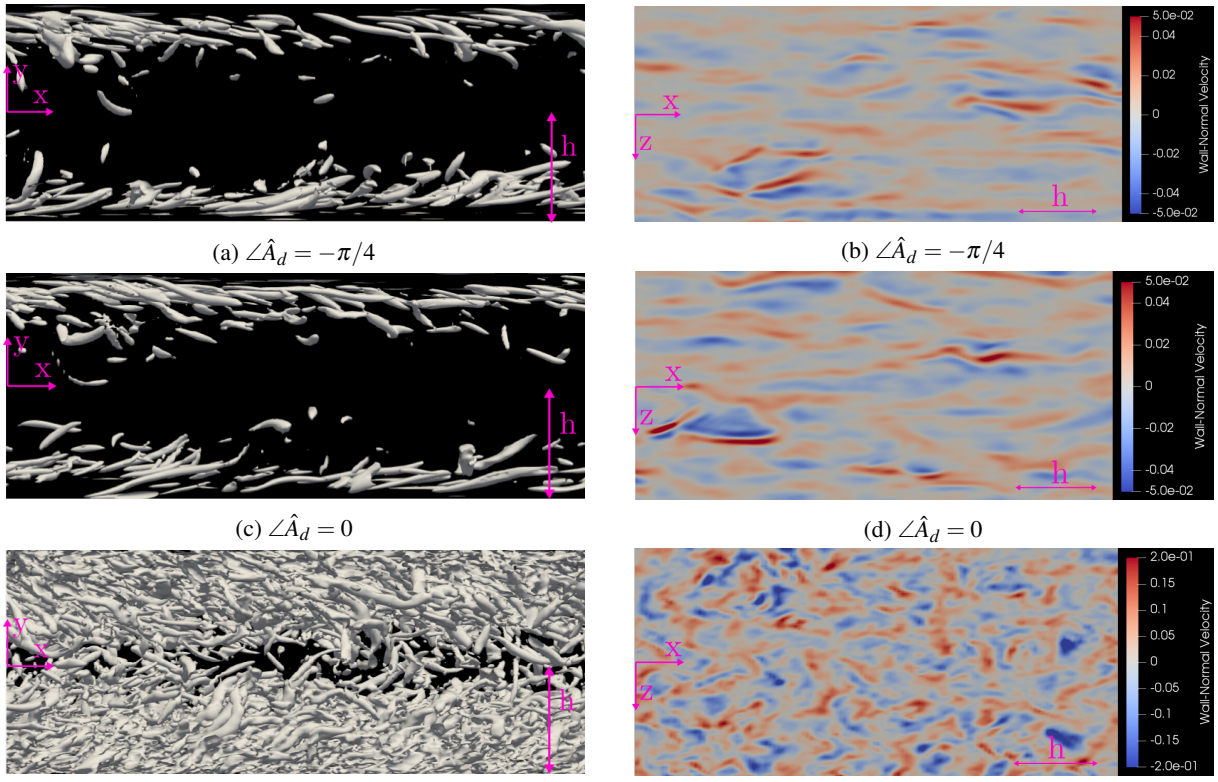

(a) $\angle\hat{A}_d = -\pi/4$ (b) $\angle\hat{A}_d = -\pi/4$

(c) $\angle\hat{A}_d = 0$ (d) $\angle\hat{A}_d = 0$

(e) $\angle\hat{A}_d = +\pi/2$ (f) $\angle\hat{A}_d = +\pi/2$

Figure 2: Flow structures and actuator input for various phase shifts $\angle\hat{A}_d$. Figs. (2a), (2c) and (2e) show streamwise wall-normal cross sections of instantaneous λ_2-isosurfaces. The threshold is $\lambda_2 = 0.05\,\lambda_u$, where $\lambda_u = -\max(|(\lambda_2)_0|)$. Figs. (2b), (2d) and (2f) display a snapshot of the actuation at the wall, $v(x, y_w, z, t)$. Note the larger magnitude of the actuator input in (2f).

ing section will support this hypothesis. The instantaneous picture also suggests that the magnitude of the actuator input is similar in both cases (note that the colorscale in both figures is the same). A more detailed analysis of the flow statistics can make this statement more precise and reveals that the wall-normal velocity fluctuations $v'(y_w)$ generated by the controller $\angle\hat{A}_d = -\pi/4$ are about 15% smaller than $v'(y_w)$ of the controller $\angle\hat{A}_d = 0$. In other words, the controller with a slightly negative phase shift achieves more DR with a smaller control input.

Fig. (2f) shows the actuator response for the controller $\angle\hat{A}_d = +\pi/2$. Instead of the streaky structure observed in the previous cases, we find a much more multiscale and unorganized control input. The streamwise coherence of the velocity signal is largely lost, but some organization is vaguely perceptible, with structures inclined with respect to the streamwise direction or even oriented along the span. It is also interesting to note that the control input is about an order of magnitude larger than in the previous cases, but the larger input results in drag increase rather than drag reduction. This suggests that the sensor measurement and actuator response lock-on and that their feedback with positive phase shift drives the flow to a new state with enhanced turbulence.

Spectral Analysis

The previous discussion about structural features has shown a close similarity between the controllers with $\angle\hat{A}_d = -\pi/4$ and $\angle\hat{A}_d = 0$. Their spectral properties are also very similar and we therefore leave out the discussion of $\angle\hat{A}_d = 0$ in this section.

Fig. 3 shows the power spectrum of the wall-normal velocity at various wall-parallel planes as a function of the streamwise (λ_x) and spanwise (λ_z) wavenumber. The left column shows the spectra of $\angle\hat{A}_d = -\pi/4$ (maximum DR), while the right column displays the spectra of $\angle\hat{A}_d = +\pi/2$ (substantial drag increase). The wall-normal locations are identical for both controllers and correspond to: actuator input at $y^+ = 0$ (first row), sensor measurement at $y^+ = 14.5$ (second row) and $y^+ = 31.0$ (third row), which is approximately the wall-normal location at which v' peaks for $\angle\hat{A}_d = +\pi/2$. The spectra were obtained by averaging the corresponding planes of the upper and lower channel half and the friction velocity of the uncontrolled flow, $(u_\tau)_0$, is used to rescale velocities and lengths to inner units. Note that the wavelengths $\lambda_x^+ < 45$ and $\lambda_z^+ < 28$ are omitted in Fig. 3. This choice was motivated by the observation that the actuator input at these small wavelengths is almost zero.

We first turn our attention to the case $\angle\hat{A}_d = -\pi/4$ shown in the left column. The power spectrum of the actuation, Fig. (3a), confirms the instantaneous observations of the previous section from a statistical point of view: the actuation signal is dominated by large streamwise structures, with the peak occurring at $\lambda_x^+ \approx 2260$ and $\lambda_z^+ \approx 103$. These scales are reminiscent of the near-wall cycle and give further evidence that the distinct spatial structure of the control signal is an imprint of the quasi-streamwise vortices. The spectrum at the sensor location, shown in Fig. (3c), is related to the spectrum at the wall through the control law (1). Under classical opposition control the two spectra would be

identical, but under varying-phase opposition control the actuator signal is less energetic than the sensor signal, as can be seen by comparing the two colorscales. This is because the controller selects the smaller of $|\hat{v}(k_x,k_z,y_d,t-\Delta t)|$ and $|\hat{v}(k_x,-k_z,y_d,t-\Delta t)|$ to generate the actuator response at $\hat{v}(k_x,\pm k_z,y_w,t)$. As mentioned earlier, this is also the reason why varying-phase opposition control with $\angle\hat{A}_d = 0$ leads to less DR than classical opposition control. The close resemblance of Figs. (3a), (3c) and (3e) further shows that the flow structure is preserved as one moves away from the wall.

The column on the right shows the corresponding spectra for the case $\angle\hat{A}_d = +\pi/2$. It is immediately apparent that many more scales are active and that the average control input is much larger compared to the case with a negative shift. It is also interesting to note that the control input is dominated by structures that are relatively short in the streamwise direction, but wide in the span. In fact, the signature of the near-wall cycle seems to be absent in the spectrum of the control signal and instead the peak actuation occurs at $\lambda_x^+ \approx 174$ and $k_z = 0$ (i.e. spanwise constant modes $\lambda_z^+ \to \infty$). The spectrum at the sensor plane, Fig. (3d), draws a similar picture, but with a peak shifted towards shorter spanwise wavelengths ($\lambda_x^+ \approx 150$, $\lambda_z^+ \approx 565$). The difference in the peak location between the sensor and the actuator spectrum is again due to the controller gain. Finally, an increased activity of larger spanwise scales compared to the $\angle\hat{A}_d = -\pi/4$ case is also observed at the peak location of v' (which for this flow occurs at $y^+ \approx 31$), as can be seen from Fig. (3f). However, it seems that more energy is transferred towards longer streamwise and shorter spanwise wavelengths as one moves away from the wall.

CONCLUSIONS

In this study we analyzed the structural and spectral changes due to varying-phase opposition control by means of DNS. We concentrated on three example controllers, all with sensors located at $y_d^+ \approx 15$: $\angle\hat{A}_d = -\pi/4$ (maximum DR), $\angle\hat{A}_d = 0$ (closely related to original opposition control scheme) and $\angle\hat{A}_d = +\pi/2$ (substantial drag increase). The structural and spectral changes observed under control with $\angle\hat{A}_d = \{-\pi/4, 0\}$ are very similar: instantaneous snapsots of the flow field and time-averaged power spectra show that both controllers attenuate the near-wall vortices and that the actuator signal bears the hallmarks of the near-wall cycle. The controller with negative phase shift is able to generate a slightly larger DR than $\angle\hat{A}_d = 0$, with smaller control input. The structural and spectral analysis further shows that controllers with a positive phase, which lead to drag increase, fundamentally change the flow structure not only in the near-wall region, but well beyond. The typical near-wall cycle scales only play a minor role and structures with large spanwise extent are much more energetic than typically observed in uncontrolled flows. Furthermore, an increased vortical activity is observed throughout the flow.

The present results show that the flow structure strongly changes with the phase of the actuator, which ultimately results in the wide variety of observed DR behavior. In the presence of numerous active spatial scales it is difficult to study how a phase shift affects a single scale and how the nonlinearity percolates the effects through the entire system. Future studies will therefore investigate the effect of a phase shift on a single scale and results form the present study can help identifying interesting target scales: the maximum DR case suggests to focus on length scales associated with the near-wall cycle, as one may expect. However, controlled flows with increased drag suggest that shorter scales with larger spanwise extent may be interesting candidates, too, since they are strongly amplified in the presence of a positive phase.

A better understanding of the phase shift for a single scale and how a single scale can affect the entire flow through nonlinear interactions may help devise effective control schemes with relaxed spatial resolution requirements and, as was shown for $\angle\hat{A}_d = -\pi/4$, reduced control inputs.

REFERENCES

Choi, Haecheon, Moin, Parviz & Kim, John 1994 Active turbulence control for drag reduction in wall-bounded flows. *Journal of Fluid Mechanics* **262**, 75–110.

Deng, Bing-Qing, Huang, Wei-Xi & Xu, Chun-Xiao 2016 Origin of effectiveness degradation in active drag reduction control of turbulent channel flow at Re_τ = 1000. *Journal of Turbulence* **17** (8), 758–786.

Flores, Oscar & Jiménez, Javier 2006 Effect of wall-boundary disturbances on turbulent channel flows. *Journal of Fluid Mechanics* **566**, 357–376.

Gad-el-Hak, Mohamed 2000 *Flow Control: Passive, Active, and Reactive Flow Management*. Cambridge University Press.

Jeong, Jinhee & Hussain, Fazle 1995 On the identification of a vortex. *Journal of Fluid Mechanics* **285**, 69–94.

Kim, Euiyoung & Choi, Haecheon 2017 Linear proportional–integral control for skin-friction reduction in a turbulent channel flow. *Journal of Fluid Mechanics* **814**, 430–451.

Lee, Jungil 2015 Opposition control of turbulent wall-bounded flow using upstream sensor. *Journal of Mechanical Science and Technology* **29** (11), 4729–4735.

Toedtli, Simon, Luhar, Mitul & McKeon, Beverley 2019 Predicting the response of turbulent channel flow to varying-phase opposition control: resolvent analysis as a tool for flow control design. Submitted.

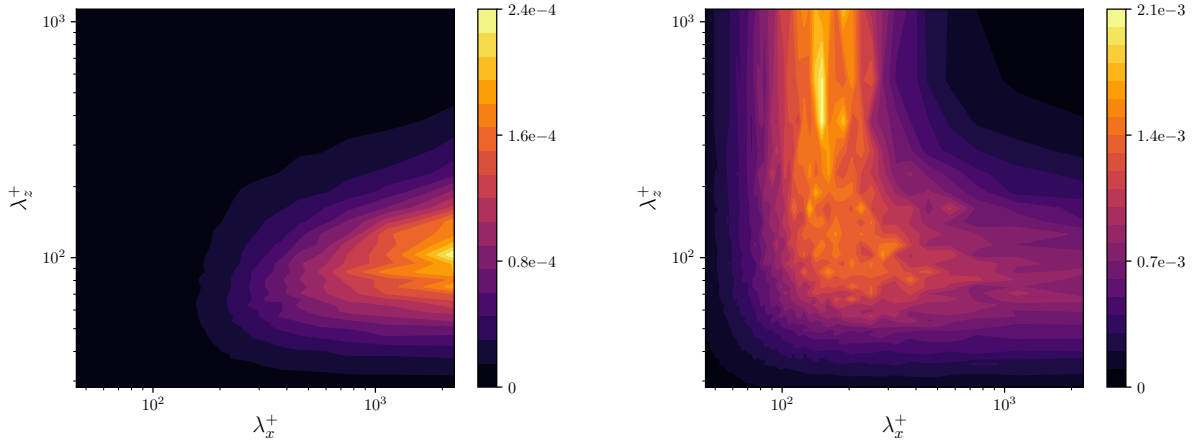

(a) $\angle\hat{A}_d = -\pi/4$, plane $y^+ = 0$

(b) $\angle\hat{A}_d = +\pi/2$, plane $y^+ = 0$

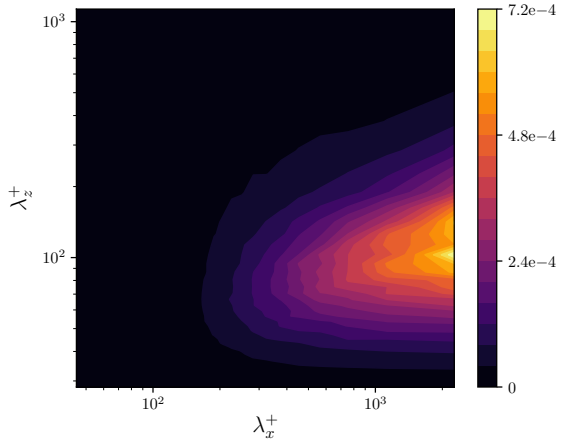

(c) $\angle\hat{A}_d = -\pi/4$, plane $y^+ = 14.5$

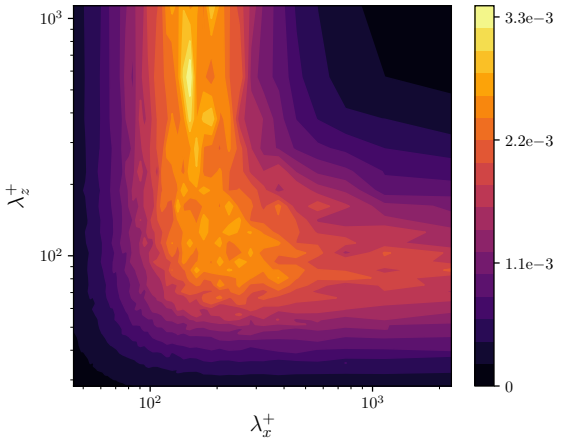

(d) $\angle\hat{A}_d = +\pi/2$, plane $y^+ = 14.5$

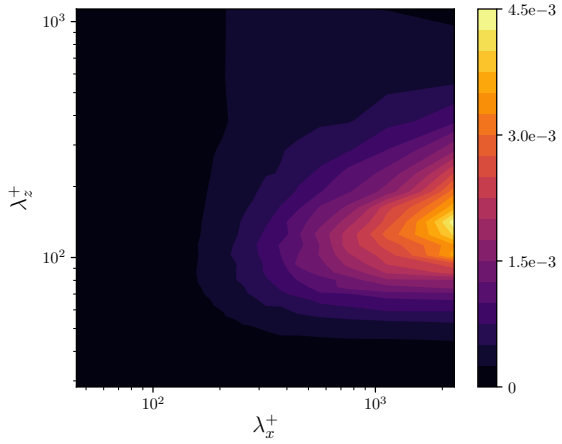

(e) $\angle\hat{A}_d = -\pi/4$, plane $y^+ = 31.0$

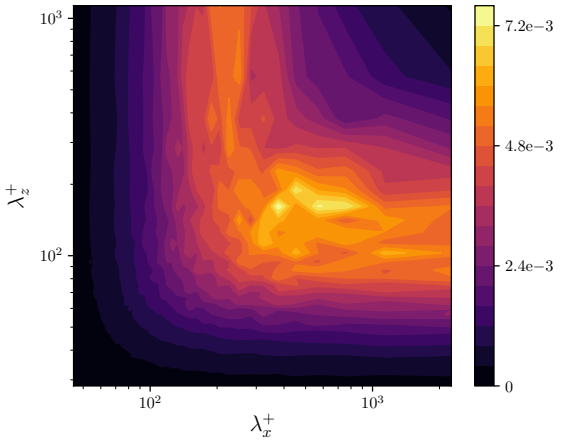

(f) $\angle\hat{A}_d = +\pi/2$, plane $y^+ = 31.0$

Figure 3: Power spectrum $\Phi_{vv}/(u_\tau^2)_0$ of the wall-normal velocity as a function of the streamwise (λ_x) and spanwise (λ_z) wavenumber at various wall-parallel planes. $\angle\hat{A}_d = -\pi/4$ for Figs. (3a), (3c) and (3e), while $\angle\hat{A}_d = +\pi/2$ in Figs. (3b), (3d) and (3f). Figs. (3a), (3b) show the actuator input, (3c) and (3d) display the sensor measurement and Figs. (3e), (3f) show the spectrum around the peak in v'. In all cases, the sensor is located at $y_d^+ \approx 15$ and the uncontrolled $(u_\tau)_0$ is used for normalization. Note that the colorscale is different in each figure.